

A wafer-scale backplane-assisted resonating nanoantenna array SERS device created by tunable thermal dewetting nanofabrication

This content has been downloaded from IOPscience. Please scroll down to see the full text.

2014 Nanotechnology 25 145304

(<http://iopscience.iop.org/0957-4484/25/14/145304>)

View [the table of contents for this issue](#), or go to the [journal homepage](#) for more

Download details:

IP Address: 192.17.144.111

This content was downloaded on 07/04/2014 at 16:18

Please note that [terms and conditions apply](#).

A wafer-scale backplane-assisted resonating nanoantenna array SERS device created by tunable thermal dewetting nanofabrication

Te-Wei Chang¹, Manas Ranjan Gartia^{1,2}, Sujin Seo^{1,3}, Austin Hsiao^{1,4} and Gang Logan Liu^{1,4}

¹ Department of Electrical and Computer Engineering, Micro and Nanotechnology Laboratory, University of Illinois at Urbana Champaign, Urbana, IL, 61801, USA

² Department of Nuclear, Plasma, and Radiological Engineering, University of Illinois at Urbana Champaign, Urbana, IL, 61801, USA

³ Department of Material Science and Engineering, University of Illinois at Urbana Champaign, Urbana, IL, 61801, USA

⁴ Department of Bioengineering, University of Illinois at Urbana Champaign, Urbana, IL, 61801, USA

Received 23 October 2013, revised 28 December 2013

Accepted for publication 15 January 2014

Published 14 March 2014

Abstract

A tunable lithography-less nanofabrication process using a metal thin-film thermal dewetting technique has been developed to fabricate wafer-scale and uniform plasmonic substrates at low cost for optimal performance in surface enhanced Raman scattering (SERS) applications. The relationship between the tunable parameters of this process and the corresponding optical and plasmonic characteristic is investigated both experimentally and theoretically to understand the deterministic design of an optimal SERS device with a three-dimensional plasmonic nanoantenna structure. The enhancement of SERS using various nanoplasmonic particle sizes, structure lengths, lateral hot spot spacings and resonating effects are examined and demonstrated. We achieve a uniform optimal enhancement factor of 1.38×10^8 on a 4 in wafer-scale SERS substrate with a backplane-assisted resonating nanoantenna array design. Sensitive environmental nitrate sensing, vitamin detection and oligonucleotide identification are demonstrated on the high-performance SERS device.

Keywords: nanofabrication, thermal dewetting, surface enhanced Raman scattering (SERS), backplane-assisted resonating nanoantenna array (BARNA), ultra-sensitive detection

 Online supplementary data available from stacks.iop.org/Nano/25/145304/mmedia

(Some figures may appear in colour only in the online journal)

1. Introduction

Nanometer scale metal particles have attracted considerable attention in recent decades because of their unique optical properties compared with traditional bulk materials. The plasmonic phenomenon of metal nanoparticles has shown significant advantages in various applications such as nanofabrication [1], optical communication [2] and biological sensing

[3, 4]. Owing to the extraordinary electromagnetic field enhancement from localized surface plasmon resonance (LSPR), surface enhanced Raman scattering (SERS) on metal nanoparticles is considered to be a powerful analytical tool in biological and chemical studies for understanding molecular information such as chemical bonding, composition and crystal orientation [5]; these can be identified precisely by the frequency shift in the scattering spectrum [6].

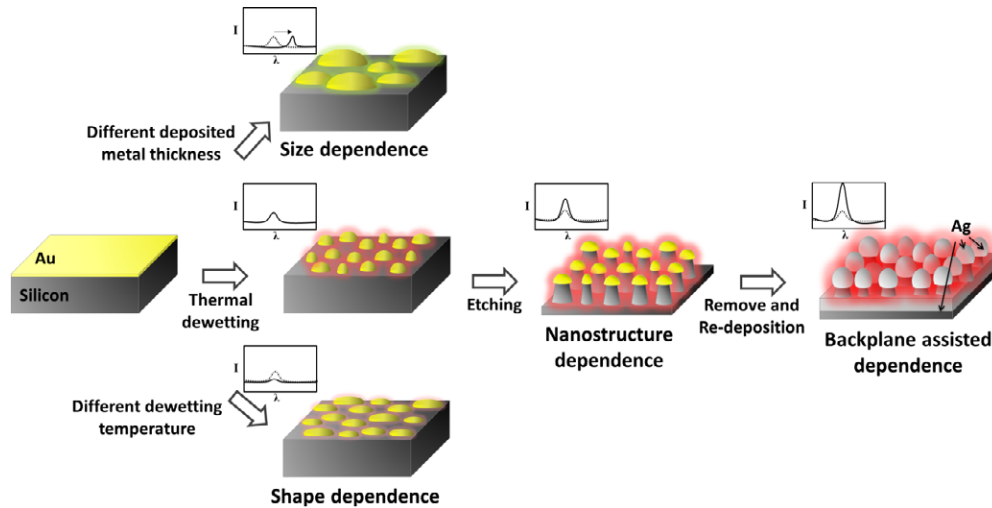


Figure 1. Overview of plasmonic enhancement with different process dependences including the morphology of the metal nanoparticles, the appearance of the nanostructure and the backplane-assisted effect.

Researchers have used different approaches to obtain high-sensitivity SERS substrates, including both top-down and bottom-up processes. Among all top-down methods, electron-beam lithography (EBL) provides ultra-high controllability to obtain the required pattern size and position [7]. However, the inevitable time-consuming process limits its application to laboratory purposes only. Nanosphere lithography (NSL) [8] or nanoimprint lithography [9] has the similar advantages as EBL but with much higher throughput. Unfortunately, the delicate manufacturing process required makes it difficult to use these techniques to yield large-area devices. On the other hand, bottom-up synthesis of metal nanoparticle clusters [10–12] is advantageous as it can provide a way to fabricate devices with high sensitivity and is compatible with large-scale fabrication as well. Nevertheless, synthesis of such nanoparticles requires reactions with specific chemicals, making the whole process complicated and time-consuming. Besides, uniformity and controllability in the synthesized nanoparticles are rather difficult to achieve with a chemical fabrication process.

In recent years the thermal dewetting has begun to reveal its potential for low-cost nanostructure fabrication. The combination of top-down and bottom-up techniques offers an efficient way to fabricate a nanostructured surface. Thermal dewetting is based on the spinodal phenomenon on metal thin film [13–15]. Injection of thermal energy induces the thin metal layer to fluctuate and conduct bicontinuous sinusoidal thermal capillary waves. Finally the metal thin film transforms into separated particles. This method has been successfully applied to fabricate an antireflection layer on Si and III–V materials for optical applications [16, 17]. Furthermore, the ability to form uniform large-area metal nanoparticle arrays using the thermal dewetting technique has been exploited to fabricate SERS substrates. However, the plenary substrate with a single plasmonic layer made by this method provided only a modest enhancement factor of about 10^6 [18]. Oh and Jeong demonstrated high SERS enhancement by applying a thermal dewetted metal particle pattern as a mask to fabricate

SiO_2 nanostructures [19]. After glancing angle deposition, the silver metal layer was deposited on the top and sidewall of the nanostructures. They achieved an enhancement factor of the order of 10^7 experimentally due to the three-dimensional (3D) dielectric structure with a higher density single plasmonic layer. However, the optical characteristic of this substrate was not fully discussed and the underlying mechanism of the difference between plane and structured thermal dewetting substrates is not clear so far. Moreover, the position and size of the sidewall particles are randomized and not controllable.

In this paper we demonstrate a deterministic process based on a thermal dewetting technique to fabricate a large-area, low-cost plasmonic substrate for ultra-sensitive SERS sensing applications and discuss the correlation between the plasmonic enhancement and tunable parameters of the process in detail. It is shown that the plasmonic resonant frequency and intensity can be easily tuned by modulating the morphology of the metal nanoparticles, the appearance of the nanostructure and using the backplane-assisted coupling effect in this process. The overview of plasmonic effects to their dependences is shown in figure 1. The significant enhancement is due to the novel backplane-assisted resonating nanoantenna array (BARNA) design, which is a metal backplane underlying a metal nanoparticle array supported by silicon nanostructures. The enhanced lateral coupling and increased hot spot region have been shown to be shown advantageous in improving the scattered field of the Raman signal. The optimized plasmonic device for SERS is identified through numerical analysis and validated experimentally. A high SERS enhancement factor ($>1.38 \times 10^8$) is demonstrated in the detection of nitrate ions, vitamin molecules and sensitive identification of DNA molecules.

2. Methods

2.1. Sample preparation

The substrate used in the work described in this paper is 4'' single crystalline p-type doped silicon wafer. The crystalline

orientation is $\langle 1, 0, 0 \rangle$ and the resistivity is $0.2\text{--}0.5 \Omega \text{ cm}^{-1}$. All the substrates were cleaned with acetone, isopropyl alcohol and deionized water before proceeding with any further fabrication steps. The native oxide layer was intentionally kept in order to give better adhesion for further processes. A comparison between the situation with and without a native oxide layer can be found in the supplementary data (available at stacks.iop.org/Nano/25/145304/mmedia). Then different thicknesses of gold thin film (5, 7.5 and 10 nm) were deposited on the substrate by a Temescal six pocket electron-beam evaporation system for the thermal dewetting process.

2.2. Thermal dewetting process

In order to perform thermal dewetting, a Jipelec rapid thermal processor was used to inject thermal energy into a gold thin film and induce thermal disturbance. The advantage of the rapid thermal process (RTP) system is that it significantly reduces the heating time and enables the process to be finished within 5 min. The chamber was purged with nitrogen gas into to prevent any oxidation occurring during whole process. The dewetting temperature varied from 100 to 500 °C for 90 s.

2.3. Nanofabrication process

After thermal dewetting, the pattern of metal nanoparticles was transferred by dry etching. In this step, a STS Advanced Silicon Etch system was used for inductively coupled plasma reactive ion etching (ICP-RIE). A high aspect ratio structure can be achieved by continuously applying etching and passivation processes. SF_6 and O_2 were used for the etching phase and C_4F_8 was used for the passivation process. The pressure was set to 100 mTorr and the RF powers of the inductive and capacitive chambers were set to be 600 and 12 W, respectively. To further improve the the field enhancement, metal nanoparticles were removed by placing the sample into a gold etcher for 5 min and then silver was deposited by a CHA SEC-600 electron-beam evaporator system. The power of the electron beam was 10 kV and the operating pressure was around 10^{-7} mTorr. The evaporation rate was set to 0.5 \AA s^{-1} to ensure uniformity of the silver layer. The deposited thicknesses were varied from 20 to 140 nm in order to find the optimal SERS performance.

2.4. Reflectance measurement

In order to understand the plasmonic properties and light-trapping phenomena of this device, optical reflectance was measured by a Varion Cary 5G UV-vis-NIR spectrophotometer. An integrated sphere was used to collect all the scattered light to ensure accurate data and the wavelength range was from 300 to 1100 nm.

2.5. SERS measurement

A Renishaw PL/Raman micro spectroscopy system was used for the measurement of Raman spectra. A $20\times$ objective lens was used for focusing and collecting the incident laser and

Raman signals. The wavelength of the excitation light source was 633 and 785 nm and the acquisition time was set to 10 s. The intensity of the laser was reduced to 10% of maximum intensity for 633 nm and to 0.5% of maximum intensity for 785 nm in order to prevent saturation of the detector. The measured wavenumber range was from 700 to 1100 cm^{-1} .

2.6. Numerical simulation

The electric field distribution and reflectance of the electromagnetic field through the structures were studied using the 3D finite-difference time-domain (3D-FDTD) method and implemented by FDTD software from Lumerical Solutions, Inc. A transverse magnetic (TM) polarized electromagnetic wave was set to propagate normal to the substrate for both diffuse reflectance simulation and plasmonic enhancement simulation. The boundary condition for the x and y directions was periodic to calculate the interparticle effect in periodic arrays of nanostructures and the maximum mesh size around the metal particles was 1.5 nm.

3. Results

3.1. Nanofabrication processes

Figure 2 shows the schematic and scanning electron microscopy (SEM) images of the BARNA substrate process. Firstly a 4" single crystalline silicon wafer was covered with gold thin film (several nanometers) by e-beam evaporation (figure 2(a)). After performing thermal dewetting, the gold thin film was transformed to a two-dimensional (2D) gold nanoparticle (AuNP) substrate as shown in figure 2(b). Then by applying ICP-RIE on the silicon substrate, the original metal nanoparticles are supported by silicon nanorods and the device becomes a three-dimensional AuNP substrate as shown in figure 2(c). Finally, a BARNA substrate can be obtained by removing metal and then depositing a thicker layer of silver, as shown in figure 2(d). The total processing time for the whole wafer-scale substrate was less than an hour. The inset figures in figures 2(b)–(d) show the whole 4" wafer and confirm the large-area capability and uniformity of the developed nanofabrication process.

Nanostructure tunability in our fabrication process is demonstrated in figure 3.

- (1) Nanoparticle size: based on the spinodal dewetting theory the size of the metal particle can be tailored by varying the thickness of the gold thin film layer [14]. In figures 3(a)–(c), SEM images show the size of metal particles with different gold layer thicknesses (5, 7.5 and 10 nm) after applying thermal dewetting. The corresponding particle size distributions are shown in figures 3(d)–(f). The results indicate that the thicker the metal layer is, the larger the metal nanoparticles that can be formed. The statistics have shown good agreement with theory and also proved that the size of metal nanoparticles can be controlled by the thickness of deposition.

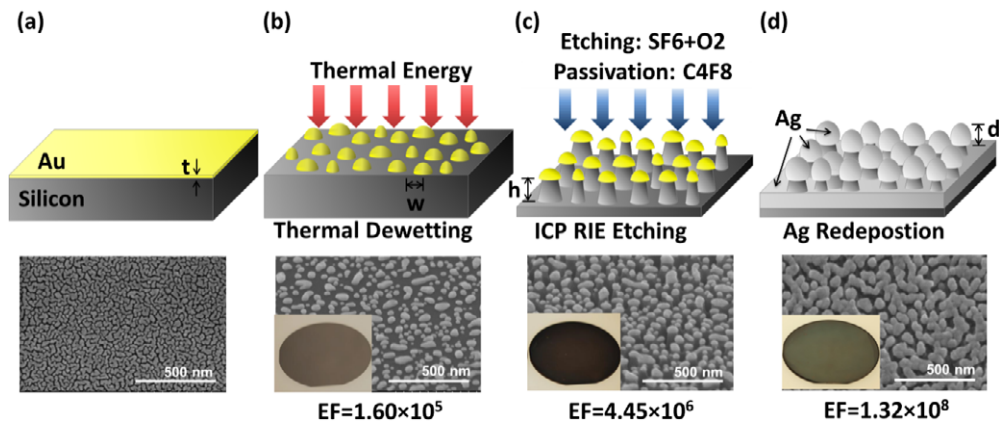


Figure 2. Schematic of the plasmonic substrate made by the BARNA process and corresponding SEM images. Insets in the SEM images are photos of a 4'' wafer in each substrate. The averaged Raman enhancement factors of each step are labeled at the bottom of the figures.

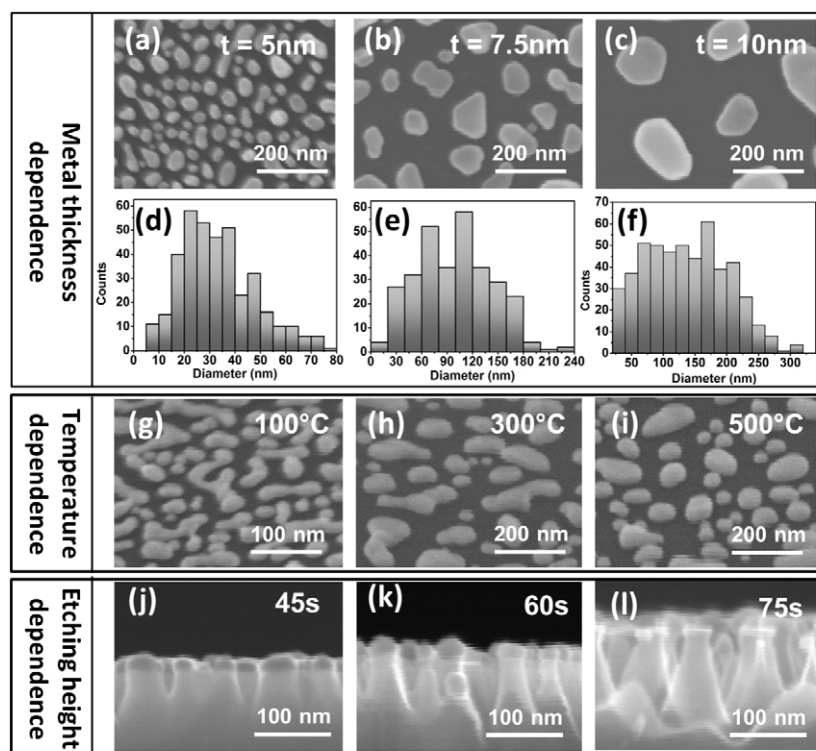


Figure 3. Controllability of different geometrical parameters. (a)–(c) SEM images of metal nanoparticles transformed from different thicknesses of gold thin film ($t = 5, 7.5$ and 10 nm); (d), (e) the corresponding statistical distribution of metal nanoparticle sizes in (a)–(c). (g)–(i) SEM images of metal nanoparticles with different thermal dewetting temperatures (temperatures of $100, 300$ and 500 °C, respectively). (j)–(l) Cross-sectional SEM images of the nanostructured substrate with different etching conditions.

- (2) Nanoparticle shape: in figures 3(g)–(i) the shape of the metal particles varies with different thermal dewetting temperatures at $100, 300$ and 500 °C, respectively, and with continuous nitrogen purging. As the temperature increases, the AuNPs become more spherical in shape from increasing particle height and decreasing particle width.
- (3) Nanorod height: figures 3(j)–(l) show that different heights of silicon nanorod can be made under different etching conditions or etching time durations. Hence the shape and diameter of the AuNPs as well as the height of

silicon nanorod can be tuned to achieve the desired 3D nanostructure device design.

3.2. Optical characteristics

In order to optimize the design of the plasmonic substrate for SERS applications with all the controllable factors discussed above, it is necessary to understand the influences of all tunable parameters on its plasmonic properties. Figure 4(a) shows the diffuse reflectance spectra of AuNPs made by thermal dewetting for two different metal film thicknesses, 5 and

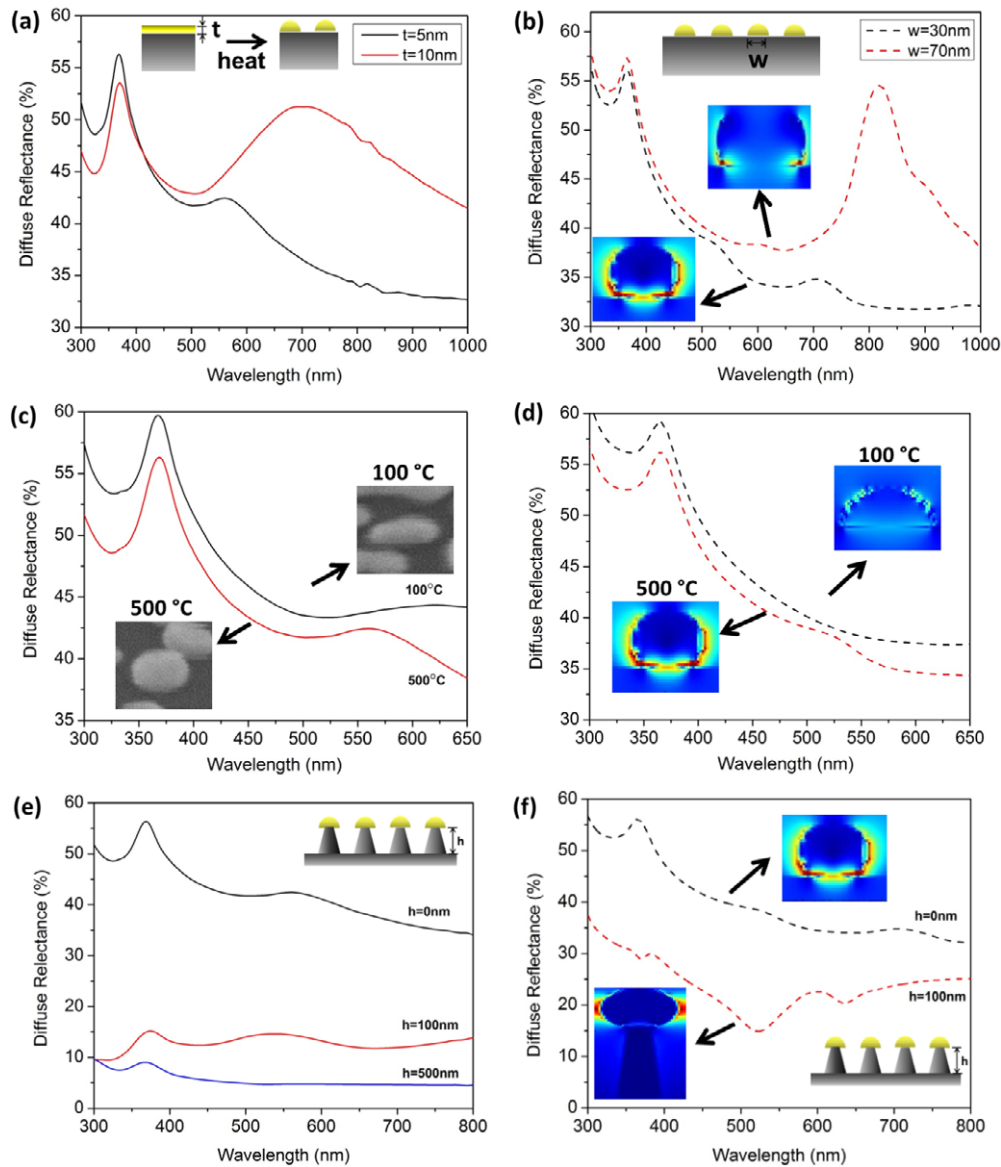


Figure 4. Optical characteristics obtained by individually varying different geometrical parameters. (a) Experimental and (b) numerical diffuse reflectance spectrum of different AuNP sizes by changing the deposited thickness. (c) Experimental and (d) numerical reflectance spectrum of different AuNP shapes by applying different thermal dewetting temperatures. (e) Experimental and (f) numerical reflectance spectrum of 3D AuNP substrates with different nanorod heights. Enlarged figures of electric field distribution can be found in supplementary information (available at stacks.iop.org/Nano/25/145304/mmedia).

10 nm. As shown in figure 3, the particle size becomes larger when the thickness of the deposited metal layer increases. The main difference between the two cases is the reflectance peak associated with the coupled LSPR red shifts from 560 to 700 nm when the dewetting thickness varies from 5 to 10 nm. In addition the coupled LSPR peak becomes broader when the thicker metal layer is applied. The reason for broadening phenomenon is that the variation of particle size is greater with thicker metal layers (as shown in figure 2). From FDTD simulation in figure 4(b) we can observe the same tendency with particle sizes of 30 and 70 nm. (Figure S1 in supplementary information available at stacks.iop.org/Nano/25/145304/mmedia shows more simulation results with various sizes of AuNPs.) As a result, the LSPR peak can be

tuned by using different metal thicknesses in order to fit the excitation laser wavelength. The insets show the electric field at 633 nm excitation in both cases, and it indicates that a 5 nm metal film is more appropriate at certain applied wavelengths where the resonance peak is closer.

The dewetting temperature dependence is shown in figure 4(c). The diffuse reflectance was measured for samples with different dewetting temperatures of 100 and 500 °C, respectively. It can be inferred from the SEM images in figure 2 that as we increase the dewetting temperature, the metal particles become more spherical. This shape difference provides different plasmonic resonance modes inside the AuNPs due to different damping attenuations. This phenomenon is verified in the FDTD simulation in figure 4(d). The insets are the

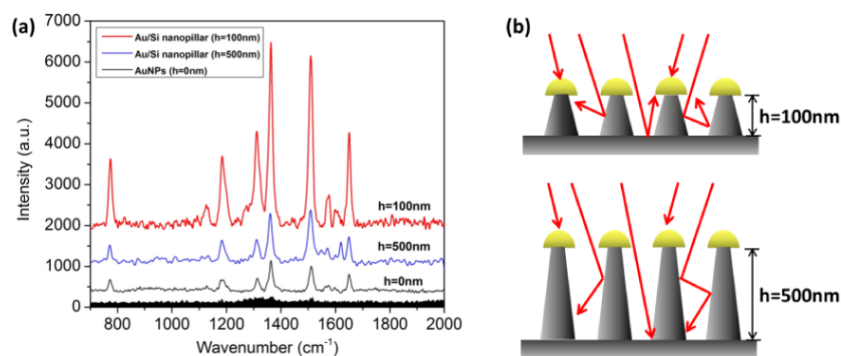


Figure 5. (a) The Raman spectrum of 100 μM R6G on 2D and 3D AuNP (height = 100 and 500 nm) substrates. The black shadow is the standard deviation of the SERS spectrum from seven different positions of the 3D AuNP plasmonic substrate with 100 nm high nanorods. (b) Schematic illustrating the propagating path of photons with shorter and longer nanostructures with a light-trapping effect.

electric field distribution at a wavelength of 633 nm for the two different dewetting temperatures and it suggests that a higher electric field and lower damping loss can be achieved in the more spherical nanoparticles produced by applying a higher dewetting temperature.

Finally, after performing the silicon etching process and forming a 3D AuNP substrate, figure 4(e) shows the diffuse reflectance measurements with various silicon etching depths of 0, 100 and 500 nm, respectively. A broadband antireflection effect can be observed when silicon nanorods appear. This is because of the light-trapping phenomenon where photons have a higher probability of eventually being absorbed by the nanostructures. This phenomenon can also be found in the FDTD simulation shown in figure 4(f). The insets show the higher electric field enhancement due to light trapping. In summary, all the geometrical properties can affect the plasmon resonance of the device including transition of the plasmonic mode or modification of the coupling efficiency.

3.3. SERS measurement of 2D and 3D AuNP substrates

For comparison, the SERS effects of both 2D and 3D AuNP substrates were noted and demonstrated. In order to calculate the Raman enhancement factor, Rhodamine 6G (R6G), a common dye used as a standard analyte for Raman measurement, was used as the probe molecule. The Raman signal of R6G was also measured on a smooth silicon wafer as the reference. A 5 nm gold deposition layer and a dewetting temperature of 500 °C were chosen intentionally to match the excitation laser wavelength of 633 nm in our Raman spectroscopy system. Figure 5(a) shows the Raman spectrum of 100 μM R6G on 2D and 3D AuNP substrates. Two different heights of silicon nanorod, 100 and 500 nm, were used. Here, 0 nm indicates the case without etching (2D AuNPs). The shape and size of the AuNPs are assumed to be identical in all three cases since the same processing conditions were applied. According to the results, the peak intensities of the Raman signal on the nanostructured substrate are larger than with a plane substrate. The reason for this is the light-trapping effect of the nanostructure, which agrees with the results for a FDTD simulated electric field shown in the previous section. This indicates that incident photons can be more efficiently coupled

to the 3D plasmonic structure with light-trapping nanorods to excite the molecules.

When comparing the results for different nanorod heights, the nanostructure with 100 nm silicon nanorods shows higher enhancement than the one with 500 nm nanorods, which is contradictory to the optical absorbance result (the absorbance of the substrate with 500 nm nanorods is greater than that of the substrate with 100 nm nanorods). The possible reason is that when photons are incident on the substrate and are bounced within the nanostructures, the substrate with the shorter rods (substrate height 100 nm) has a greater probability the photons being absorbed by AuNPs instead of silicon. Figure 5(b) is a schematic of explaining this difference in absorbance between longer and shorter nanorods. The shadowed area in figure 5(a) is the standard deviation of the Raman intensity measurement at seven different positions within one sample. This result indicates that the Raman intensity has a high uniformity across the substrate. By calculation, the averaged SERS enhancement factors of 2D and 3D AuNP substrates with a 100 nm pillar height are 1.60×10^5 and 4.45×10^6 , respectively. The signal is enhanced by around 28 times by simply fabricating the silicon nanorod array underneath the same metal nanoparticles. The 3D AuNP substrate has a similar order of enhancement as a commercially available Klarite SERS substrate while using much less gold for layer deposition, and was able to detect concentrations of R6G as low as 1 μM (see supplementary information available at stacks.iop.org/Nano/25/145304/mmedia).

3.4. SERS optimization of BARNA plasmonic substrate

In order to achieve higher enhancement, proper design of the 3D plasmonic structure with tightly packed ‘hot spots’ is necessary for the SERS substrate. A ‘hot spot’ is defined as the gap between two individual metal particles, which exhibits a high coupling electric field to enhance the Raman intensity. The smaller the gap (but not interconnected) between particles that can be achieved, the higher the SERS effect can be induced [20]. FDTD simulation in figure 6(a) shows the differences in the electric field distribution for different sizes of AgNPs where the periodicity of the nanorods stays the same. It can be observed that the enhancement is largest when

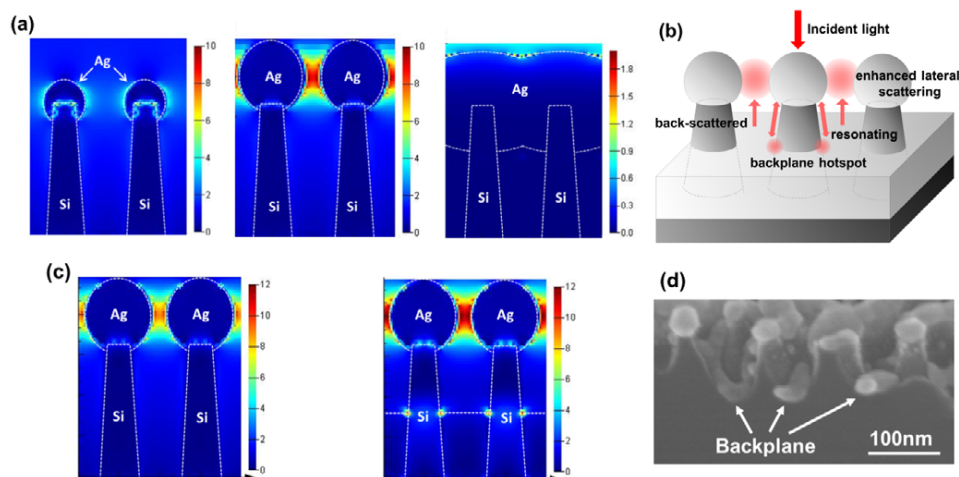


Figure 6. (a) FDTD simulations of the electric field distribution for different sizes of metal nanoparticles on a 3D AgNP substrate. (b) Illustration of the enhanced scattering field assisted by the metal backplane. (c) FDTD simulations of electric field distribution with and without a metal backplane on a 3D AgNP substrate. (d) Cross-sectional SEM image of the BARNA substrate. The excitation wavelength of all FDTD simulations above is 633 nm.

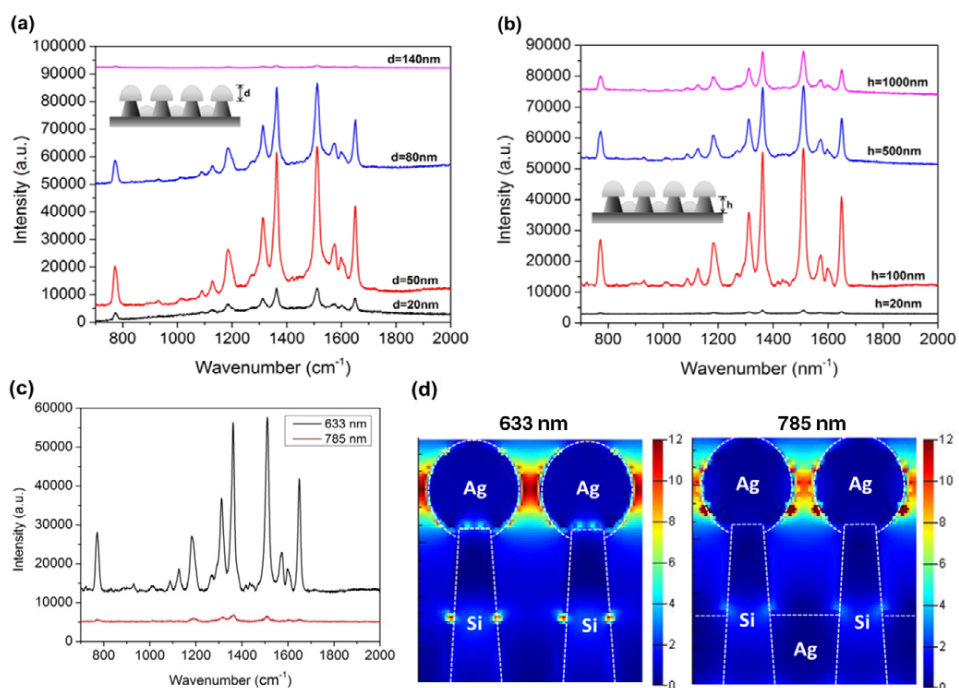


Figure 7. (a) SERS spectrum of 100 μ M R6G on a BARNA substrate with different Ag thicknesses ($d = 20, 50, 80$ and 140 nm). (b) SERS spectrum of 100 μ M R6G on a BARNA substrate with different etching heights ($h = 20, 100, 500$ and 1000 nm). (c) SERS spectrum of 100 μ M R6G on AN optimized BARNA substrate (50 nm silver deposition and 100 nm pillar height) with different excitation wavelengths (633 and 785 nm). The power of both lasers source is the same. (d) FDTD simulation of the electric field distribution with different excitation wavelengths on a BARNA substrate.

the AgNPs are separated by ultra-small gaps. Besides that, by placing an additional metal layer around the bottom of the silicon nanorods, a backplane metal layer can be created which helps to further enhance the Raman signal. The advantages of a backplane are: (1) it reflects the back-scattered field instead of it being absorbed by silicon; (2) it provides additional hotspot regions around the silicon nanorods; and (3) it creates a resonating cavity with metal nanoparticles and increases the lateral coupling field (illustrated in figure 6(b)). These advantages can be observed by comparison of FDTD simu-

lations in figure 6(c), and the resonating effect has also been observed by other researchers with similar configurations [21, 22]. The BARNA substrate can be achieved by the following processes: after fabrication of the 3D AuNP substrate, the top gold layer is removed from the silicon nanorods and a new silver layer deposited on the nanostructured silicon surface (detailed schemes can be found in supplementary information available at stacks.iop.org/Nano/25/145304/mmedia). From the SEM images in figure 6(d), we can clearly observe that

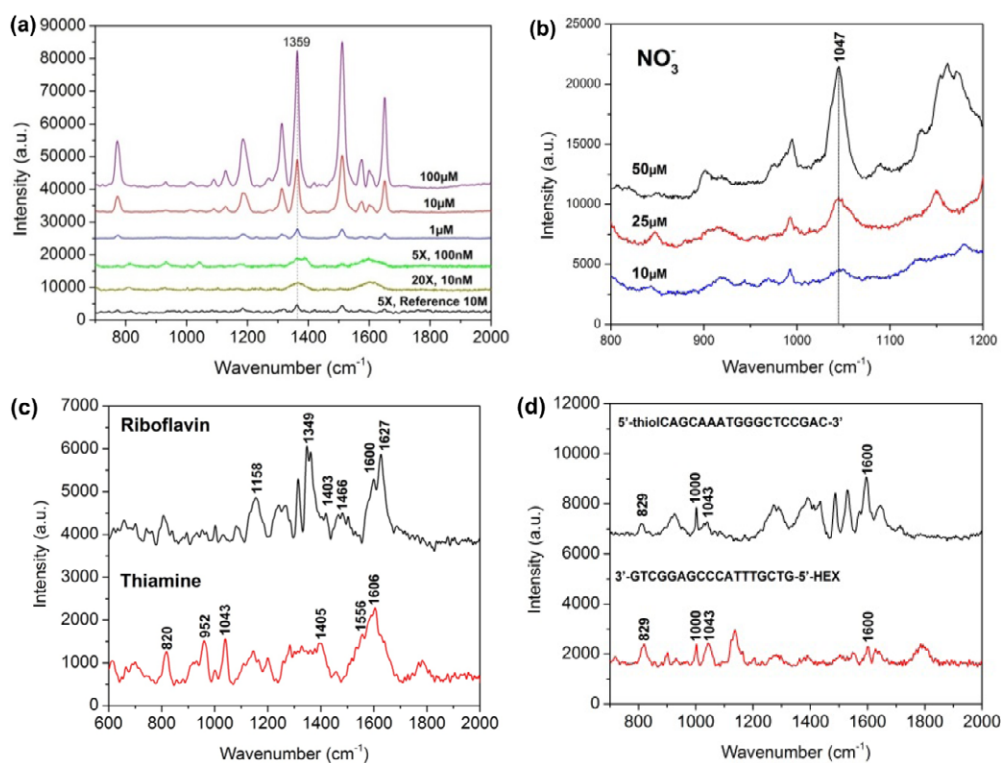


Figure 8. SERS spectrum of (a) different concentrations of R6G (from 100 μM to 10 nM); (b) different concentrations of nitrate (10.25 and 50 μM); (c) 100 nM riboflavin and thiamine; and (d) two single-stranded DNAs, 5'-thiolCAGCAAATGGGCTCCGAC-3' and 3'-GTCGGAGCCCATTGCTG-5'-HEX with 1 nM with a BARNA substrate applied. All spectra were obtained by averaging three different measurements.

silver is deposited at two different levels and the backplane is located below the silicon nanorods.

Figure 7 shows the optimization of the BARNA substrate. Firstly, different thicknesses of silver (20, 50, 80 and 140 nm) were deposited on the nanostructured substrate with a nanorod height of 100 nm. The average SERS intensity for a 633 nm excitation wavelength was measured and is shown in figure 7(a). The highest SERS enhancement was obtained from the substrate with a silver thickness of 50 nm. The SEM images in the supplementary information (figure S6 available at stacks.iop.org/Nano/25/145304/mmedia) show the differences in the nanoparticle spacing due to the change in deposition thickness and confirm that the substrate with a metal thickness of 50 nm produces nanogaps between nanoparticles and thus more hot spots than the other thicknesses. Secondly, samples with different structure heights (100, 500 and 1000 nm) were deposited with a 50 nm silver layer and the SERS intensity was measured on each substrate, as shown in figure 7(b). Clearly, the substrate with a nanorod height of 100 nm provides the highest enhancement. The reason for this should be that the plasmonic coupling only happens when two metal–dielectric interfaces are sufficiently close to each other [22]. Besides that, we also found that this optimized design (50 nm silver deposition and 100 nm pillar height) has better SERS enhancement with an excitation wavelength of 633 nm than with 785 nm as shown in figure 7(c). From figure 7(d), the FDTD simulations with different excitation wavelengths infers that 633 nm has better resonance both in lateral coupling of top AgNPs and in a metal backplane around the silicon nanorods.

Different concentrations of R6G (from 100 μM to 10 nM) have been unambiguously detected with the optimized BARNA substrate (50 nm silver deposition and 100 nm pillar height), as shown in figure 8(a). A low concentration such as 10 nM can be routinely detected, which points to the significant high enhancement factor achievable with this design. An average enhancement factor of 1.38×10^8 uniformly across the wafer surface was obtained using the optimized BARNA device, which is a further improvement of 30 times compared to the 3D AuNP substrate. The stability of the BARNA SERS substrate was examined by placing the substrate in air for a month. Although the SERS ability degrades due to the formation of silver oxide, it still remains at the same order of magnitude as a freshly prepared substrate. (Please see supplementary information for comparison data, available at stacks.iop.org/Nano/25/145304/mmedia.)

3.5. SERS detection of chemicals and biomolecules using the optimized substrate

The optimized BARNA substrate was used to detect several biologically and environmentally relevant chemicals and ions. For example, the nitrate (NO_3^-) ion is a stable form of nitrogen commonly found in environmental water such as stream water, rivers or lakes. Since the fertilizers used in agriculture usually contains nitrogen compounds, the concentration of nitrate in water will be significantly different according to agricultural activities. The more fertilizers we use, the more nitrate will be dissolved in water and hence there will be an increased

concentration of nitrate in the environmental water. By sensing the nitrate concentration in water on a field we can precisely control the amount of fertilizer we should apply depending on weather and soil conditions. Also nitrate is directly related to environmental pollution and human health [23]. Figure 8(b) shows that the Raman peak intensity of nitrate changes with different nitrate concentrations (50, 25 and 10 μM) [24]. It shows that this substrate can detect much lower nitrate concentration than the US Environmental Protection Agency (EPA) maximum allowance of 10 ppm or 0.7 mM.

Next, more complicated chemicals such as B-group vitamins were detected on the optimized SERS substrate. B-group vitamins such as riboflavin and thiamine are significant elements in cell metabolism as cofactors of some key enzymes. The detection of such vitamins in body fluids has tremendous potential in pharmacokinetics. According to previous research, the concentrations of these two vitamins in human blood are in the 100 nM range [25]. Figure 8(c) shows the SERS spectra of both 100 nM riboflavin and thiamine solutions. The peak positions in both vitamins have good agreement with the reported data in previous literature [26, 27]. In addition nucleic acids such as DNA has been detected, as shown in figure 8(d). Here we use two different kinds of single-stranded DNA, 5'-thiolCAGCAAATGGGCTCCGAC-3' and 3'-GTCGGAGCCCATTTGCTG-5'-HEX, at a concentration of 1 nM. The SERS spectra of both DNAs have their own distinctive peaks and some of them (such as peaks at 1298, 1400, 1502, 1532 and 1623 nm) are identical to the Raman peaks of nucleic acid bases themselves reported in previous literature [28, 29]. This demonstrates the ability of the optimized BARNA substrate to detect and distinguish low concentrations of DNA.

4. Conclusion

We present the controllability and flexibility of a thermal dewetting technique to fabricate plasmonic device for SERS application. The correlations between plasmonic phenomena and corresponding tunable geometric parameters are thoroughly discussed based on optical characteristics and FDTD simulations. We demonstrated that the size, shape and appearance of the supported nanostructure can affect the plasmonic properties significantly. With a thicker deposited Au layer, the thermal dewetted AuNP become larger and cause a red-shift in the LSPR mode. A higher dewetting temperature provides more thermal energy to form spherical shaped AuNPs which hold LSPR better. A nanostructured substrate induces a light-trapping effect near the surface and enhances the electric near field. With the optimal backplane-assisted resonating nanoantenna array (BARNA) substrate, an enhancement factor of 1.38×10^8 can be achieved due to the high density of hot spots and enhanced scattering field from the metal backplane assistance. Finally, biologically relevant chemicals with different structural complexities, including nitrate, vitamins and DNAs, were detected with the optimized BARNA substrate to demonstrate its capability for general biological sensing applications. It shows potential for the realization of more complicated biological and chemical analyses, such as kinetic analysis of DNA hybridization, using this low-cost and high-sensitivity BARNA SERS substrate.

Acknowledgment

Some of the work was performed under the auspices of the US Department of Energy by Lawrence Livermore National Laboratory under contract DE-AC52-07NA27344. LLNL-JRNL-617411.

References

- [1] Pan L et al 2011 *Sci. Rep.* **1** 175
- [2] Maier S A and Atwater H A 2005 *J. Appl. Phys.* **98** 011101
- [3] Camden J P, Dieringer J A, Wang Y, Masiello D J, Marks L D, Schatz G C and Van Duyne R P 2008 *J. Am. Chem. Soc.* **130** 12616
- [4] Thanh N T K and Rosenzweig Z 2002 *Anal. Chem.* **74** 1624
- [5] Kneipp K, Kneipp H and Kneipp J 2006 *Acc. Chem. Res.* **39** 443
- [6] Willets K A and Van Duyne R P 2007 *Annu. Rev. Phys. Chem.* **58** 267
- [7] Duan H, Hu H, Kumar K, Shen Z and Yang J K W 2011 *ACS Nano* **5** 7593
- [8] Zhao Y, Zhang X-J, Ye J, Chen L-M, Lau S-P, Zhang W-J and Lee S-T 2011 *ACS Nano* **5** 3027
- [9] Yoo H-W, Jung J-M, Lee S-K and Jung H-T 2011 *Nanotechnology* **22** 095304
- [10] Lim D-K, Jeon K-S, Kim H-M, Nam J-M and Suh Y-D 1998 *J. Korean Phys. Soc.* **33** 292
- [11] Contreras-Cáceres R, Abalde-Cela S, Guardia-Girós P, Fernández-Barbero A, Pérez-Juste J, Alvarez-Puebla R A and Liz-Marzán L M 2011 *Langmuir* **27** 4520
- [12] Cho W J, Kim Y and Kim J K 2012 *ACS Nano* **6** 249
- [13] Bischof J, Scherer D, Herminghaus S and Leiderer P 1996 *Phys. Rev. Lett.* **77** 1536
- [14] Sharma A and Khanna R 1998 *Phys. Rev. Lett.* **81** 3463
- [15] Seemann R, Herminghaus S and Jacobs K 2001 *Phys. Rev. Lett.* **86** 5534
- [16] Leem J W, Yu J S, Song Y M and Lee Y T 2011 *Sol. Energy Mater. Sol. Cells* **95** 669
- [17] Leem J W and Yu J S 2011 *Thin Solid Films* **519** 3792
- [18] Liao T Y, Lee B Y, Lee C W and Wei P K 2011 *Sensors Actuators B* **156** 245
- [19] Oh Y J and Jeong K H 2012 *Adv. Mater.* **24** 2234
- [20] Qin L, Zou S, Xue C, Atkinson A, Schatz G C and Mirkin C A 2006 *Proc. Natl Acad. Sci. USA* **103** 13300
- [21] Li W-D, Ding F, Hu J and Chou S Y 2011 *Opt. Express* **19** 3925
- [22] Wang S, Pile D F P, Sun C and Zhang X 2007 *Nano Lett.* **7** 1076
- [23] Gartia M R, Braunschweig B, Chang T-W, Moinzadeh P, Minsker B S, Agha G, Wieckowski A, Keefer L L and Liu G L 2012 *J. Environ. Monit.* **14** 3068
- [24] Mosier-Boss P A and Lieberman S H 2000 *Appl. Spectrosc.* **54** 1126
- [25] Shils M E, Shike M, Ross A C, Caballero B and Cousins R J 2006 *Modern Nutrition in Health and Disease* 10th edn (Philadelphia: Lippincott Williams & Wilkins)
- [26] Kokaislová A and Matějka P 2012 *Anal. Bioanal. Chem.* **403** 985
- [27] Leopold N, Cîntă-Pînzaru S, Baia M, Antonescu E, Cozar O, Kiefer W and Popp J 2005 *Vib. Spectrosc.* **39** 169
- [28] Koglin E, Séquaris J-M and Valenta P 1982 *J. Mol. Struct.* **79** 185
- [29] Koglin E, Séquaris J-M, Fritz J-C and Valenta P 1984 *J. Mol. Struct.* **114** 219